


Ghost hyperbolic surface polaritons in bulk anisotropic crystals

<https://doi.org/10.1038/s41586-021-03755-1>

Received: 16 February 2021

Accepted: 22 June 2021

Published online: 18 August 2021

 Check for updates

Weiliang Ma^{1,6}, Guangwei Hu^{2,3,6}, Debo Hu^{4,6}, Runkun Chen^{1,6}, Tian Sun¹, Xinliang Zhang^{1✉}, Qing Dai^{4✉}, Ying Zeng¹, Andrea Alù^{3,5✉}, Cheng-Wei Qiu^{2✉} & Peining Li^{1✉}

Polaritons in anisotropic materials result in exotic optical features, which can provide opportunities to control light at the nanoscale^{1–10}. So far these polaritons have been limited to two classes: bulk polaritons, which propagate inside a material, and surface polaritons, which decay exponentially away from an interface. Here we report a near-field observation of ghost phonon polaritons, which propagate with in-plane hyperbolic dispersion on the surface of a polar uniaxial crystal and, at the same time, exhibit oblique wavefronts in the bulk. Ghost polaritons are an atypical non-uniform surface wave solution of Maxwell's equations, arising at the surface of uniaxial materials in which the optic axis is slanted with respect to the interface. They exhibit an unusual bi-state nature, being both propagating (phase-progressing) and evanescent (decaying) within the crystal bulk, in contrast to conventional surface waves that are purely evanescent away from the interface. Our real-space near-field imaging experiments reveal long-distance (over 20 micrometres), ray-like propagation of deeply subwavelength ghost polaritons across the surface, verifying long-range, directional and diffraction-less polariton propagation. At the same time, we show that control of the out-of-plane angle of the optic axis enables hyperbolic-to-elliptic topological transitions at fixed frequency, providing a route to tailor the band diagram topology of surface polariton waves. Our results demonstrate a polaritonic wave phenomenon with unique opportunities to tailor nanoscale light in natural anisotropic crystals.

Natural crystals can exhibit extreme dielectric anisotropy, which arises when the permittivity tensor elements along orthogonal principal axes have opposite signs. These features result in polaritons (light–matter hybrid electromagnetic excitations) with a hyperbolic dispersion—that is, the polariton wavevector \mathbf{k} follows hyperbolic isofrequency contours^{1–3}. These hyperbolic polaritons were first discovered in thin layers of van der Waals crystals, such as hexagonal boron nitride (hBN)^{4–6}, alpha-phase molybdenum trioxide (α -MoO₃)^{7,8}, alpha-phase vanadium pentoxide (α -V₂O₅)⁹ and the dichalcogenide tungsten diselenide (WSe₂)¹⁰. They feature nanoscale localization of the electromagnetic energy¹¹, long polariton lifetimes¹² and enhanced photon density of states¹³, which facilitates various applications such as subdiffraction imaging^{14,15}, thermal energy transfer¹⁶, vibrational molecular sensing^{17,18}, infrared light detection¹⁹ and twisted nano-optics²⁰.

So far, two types of hyperbolic polariton have been revealed: volume-confined hyperbolic polaritons (v-HPs)^{4,5} and surface-confined hyperbolic polaritons^{21,22} (s-HPs) (also known as Dyakonov polaritons²³). v-HPs, which propagate directionally inside low-loss crystals with a purely real-valued out-of-plane wavevector, have been mostly studied in the form of waveguide modes bounded within van der Waals thin films⁴. By contrast, s-HPs—with a purely imaginary out-of-plane

wavevector—are solutions of Maxwell's equations, supported at the interface between two media, at least one of which should be anisotropic with its optic axis in the plane²³. They are characterized by a larger electromagnetic-field confinement, smaller group velocities, higher sensitivity to the environment and similarly long lifetimes compared to v-HPs²¹. s-HPs have recently been discovered at the edges of van der Waals flakes^{21,22}; however, no experiment has directly imaged s-HPs on a sample surface. The challenge in observing s-HPs is partially associated with the fact that all previous studies on two-dimensional van der Waals materials have been restricted to scenarios in which their optic axis is either in-plane or out-of-plane, owing to the challenge in post-processing the lattice orientation of the optic axis in thin films after their exfoliation from the bulk. As such, the possible propagation features of the resulting polaritons are inevitably limited.

Here we explore the scenario in which the optic axis of a bulk anisotropic crystal and its surface are not aligned, revealing the existence of unusual anisotropic polaritons, known as ghost hyperbolic phonon polaritons (g-HPs). These light–matter hybrid quasiparticles arise from the coupling of infrared photons and lattice vibrations in anisotropic polar crystals with slanted optic axis, neither parallel nor perpendicular to the crystal surface. The g-HPs are the polaritonic analogue of the

¹Wuhan National Laboratory for Optoelectronics and School of Optical and Electronic Information, Huazhong University of Science and Technology, Wuhan, China. ²Department of Electrical and Computer Engineering, National University of Singapore, Singapore, Singapore. ³Photonics Initiative, Advanced Science Research Center, City University of New York, New York, NY, USA.

⁴CAS Key Laboratory of Nanophotonic Materials and Devices, CAS Key Laboratory of Standardization and Measurement for Nanotechnology, CAS Center for Excellence in Nanoscience, National Center for Nanoscience and Technology, Beijing, China. ⁵Physics Program, Graduate Center, City University of New York, New York, NY, USA. ⁶These authors contributed equally: Weiliang Ma, Guangwei Hu, Debo Hu, Runkun Chen. ✉e-mail: xlzhang@mail.hust.edu.cn; daiq@nanoctr.cn; aalu@gc.cuny.edu; chengwei.qiu@nus.edu.sg; lipn@hust.edu.cn

recently predicted ghost waves²⁴—a special type of non-uniform electromagnetic wave that arises in anisotropic dielectric materials^{24–28}. These waves, which are yet to be observed experimentally, take their name from an analogy in their dispersion with ghost orbit bifurcation in the semiclassical theory of non-integrable quantum mechanical systems^{24,29}. Similarly, our g-HPs support a complex-valued out-of-plane wavevector within the crystal even in the absence of material loss. Thus, they are at the same time propagating (phase oscillating) and evanescent (exponentially decaying) inside the crystal, even when material loss is neglected. Over the crystal surface, they propagate with in-plane hyperbolic dispersion, enabling long-distance directional propagation of deeply subwavelength electromagnetic fields. Ghost phonon polaritons in layered metamaterials have been predicted in a recent theoretical work³⁰, in which their in-plane hyperbolic dispersion was not revealed.

For our experimental demonstration, we use a calcite (calcium carbonate) crystal. The optical anisotropy of this material has been studied for centuries, and it is one of the most common optical materials owing to its tunable optical birefringence via optic axis alignment³¹. Its permittivity tensor can be written as $\bar{\epsilon} = \text{diag}[\epsilon_{\perp}, \epsilon_{\parallel}, \epsilon_{\perp}]$, in which ϵ_{\parallel} and ϵ_{\perp} are the principal components parallel and perpendicular to the optic axis, respectively. They have opposite signs in the mid-infrared Reststrahlen band from 1,410 to 1,550 cm^{-1} , $\epsilon_{\parallel} > 0$ and $\epsilon_{\perp} < 0$ (ref. ³²), yielding strongly anisotropic phonon polaritons³³. Owing to its oblique trigonal crystal lattice, the optic axis in calcite typically forms a finite angle with respect to its surface (θ , defined as the angle between the optic axis and interface) (Fig. 1a). This feature results in a unique advantage of calcite compared with other thin van der Waals layered nanomaterials: the tilted angle θ can be nontrivially and finely tuned ($0^\circ < \theta < 90^\circ$) by mechanically cutting and polishing the sample, therefore offering exquisite control of its overall polaritonic response (Methods and Extended Data Fig. 1) and in particular the emergence of ghost hyperbolic surface polaritons.

To understand the nature of g-HPs resulting from an oblique optic axis, we solve the source-free Maxwell's equations in the system of a dielectric background interfaced with the anisotropic calcite (Supplementary Information section 1). Assuming that the polariton wave in calcite, located at $z < 0$, carries a wavevector of $(k_x, k_y, -i \cdot q_z)$, its dispersion obeys

$$k_x^2 + k_y^2 - q_{z1}^2 = \epsilon_{\perp} k_0^2 \quad (1)$$

$$\frac{(k_y \cos \theta - i q_{z2} \sin \theta)^2}{\epsilon_{\perp}} + \frac{k_x^2 + (k_y \sin \theta + i q_{z2} \cos \theta)^2}{\epsilon_{\parallel}} = k_0^2 \quad (2)$$

Here, q_{z1} and q_{z2} are associated with ordinary and extraordinary modes, respectively. To avoid unphysical divergence in the far field, the branch cut choice in the Riemann surface must ensure that the real part of q_z is positive. When $\theta = 0^\circ$, the optic axis is located within the interface, and the corresponding solutions yield s-HPs that propagate along the surface with a purely real q_{z2} (refs. ^{21,22}); when $\theta = 90^\circ$, the optic axis is perpendicular to the interface, and surface waves are not supported because v-HPs have purely imaginary q_{z2} (refs. ^{4,5}). Non-trivial values of θ ($0^\circ < \theta < 90^\circ$) induce solutions with a simultaneously non-zero real and imaginary value of q_{z2} —that is, non-uniform waves—when $\epsilon_{\perp} \cos^2 \theta + \epsilon_{\parallel} \sin^2 \theta < 0$. This scenario corresponds to the emergence of g-HPs. More details are provided in Supplementary Information section 1.

To study g-HPs arising at the calcite–air interface, we first performed numerical simulations of dipole-excited polaritons on the (100) face of a semi-infinite calcite crystal (Fig. 1a, Supplementary Information section 2). The electric-field distribution above the surface shows concave wavefronts, a typical feature of in-plane hyperbolic polaritons (Fig. 1b) (real part of E_z , $\omega = 1,470 \text{ cm}^{-1}$, in which ω is the frequency). The Fourier

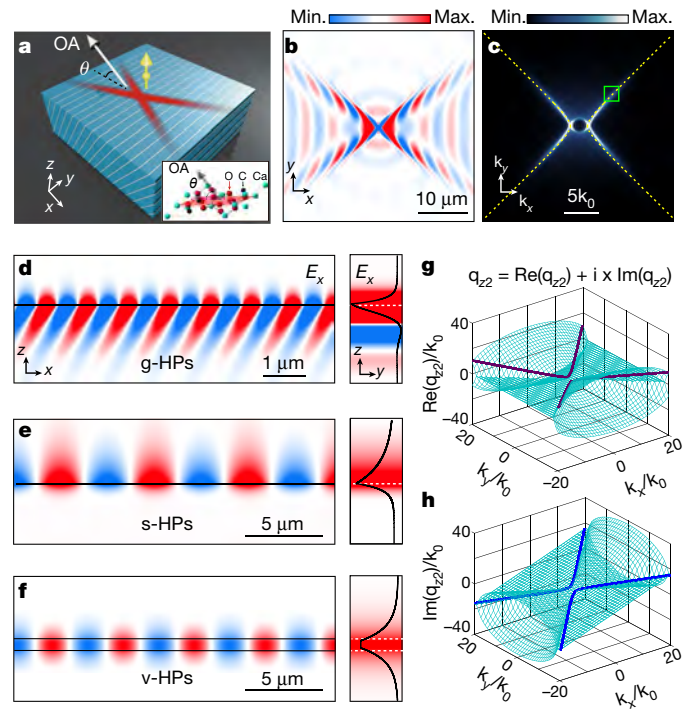


Fig. 1 | Ghost hyperbolic surface phonon polaritons at the interface of a bulk calcite crystal. **a**, Schematic of a vertical dipole launching g-HPs at the interface of a bulk crystal of calcite. The optic axis (OA) is tilted at $\theta = 23.3^\circ$ to the surface. The inset illustrates the calcite crystal structure. **b**, Simulated near-field distribution $\text{Re}(E_z)$ of dipole-launched polaritons above the surface at $\omega = 1,470 \text{ cm}^{-1}$. **c**, Absolute value of the Fourier transform of the field distribution in **b**. The dashed line shows the analytically calculated polariton dispersion. A green box denotes the g-HP mode with wavevector $|k| = 7.1k_0$, which is further analysed in **d**. **d**, Left, cross-sectional near-field distribution of the g-HP mode (marked in **c**) propagating along the surface, $\text{Re}(E_z)$. The solid black line denotes the air–calcite interface at $z = 0$. Right, the corresponding g-HP field profile in the y – z plane. **e**, Left, cross-sectional near-field distribution of an s-HP mode propagating along the surface, $\text{Re}(E_z)$. Right, the corresponding s-HP field profile in the y – z plane. **f**, Left, cross-sectional near-field distribution of a v-HP waveguide mode (the fundamental MO mode) along a thin layer, $\text{Re}(E_z)$. Right, the corresponding v-HP field profile in the y – z plane. For more details of **d**–**f**, see Supplementary Information section 2. **g**, **h**, Analytically calculated, complex-valued q_{z2} of g-HPs in calcite: the real part is shown in **g** and the imaginary part is shown in **h**. The material loss is neglected in the simulations shown in **d**–**f**, although adding the loss does not affect the results, as shown in Extended Data Fig. 4.

transform of the wavefronts reveals a hyperbolic isofrequency contour (IFC) in \mathbf{k} -space (Fig. 1c), in excellent agreement with our analytical prediction based on source-free Maxwell equations (dashed lines in Fig. 1c; Supplementary Information section 1), unambiguously demonstrating the in-plane hyperbolic dispersion of calcite polaritons. We next used a mode solver to further visualize the cross-sectional polariton field distribution (for example, for the mode with an in-plane wavevector marked in Fig. 1c; details in Supplementary Information section 2). The electric-field map corroborates the existence of surface-bound propagation of calcite polaritons (Fig. 1d), consistent with s-HPs (Fig. 1e) and distinct from v-HPs bounded within the layer (that is, waveguide modes such as the fundamental mode MO; Fig. 1f; additional details in Extended Data Figs. 2, 3). Notably, the polaritons show oblique wavefronts inside the calcite bulk, with exponential attenuation but also sinusoidal phase oscillations—a highly unusual propagation feature—totally distinct from both s-HP and v-HP. This feature is associated with the complex wavevectors q_{z2} in our analytically derived polariton dispersion, as shown in Fig. 1g, h. In these calculations we neglect material loss to

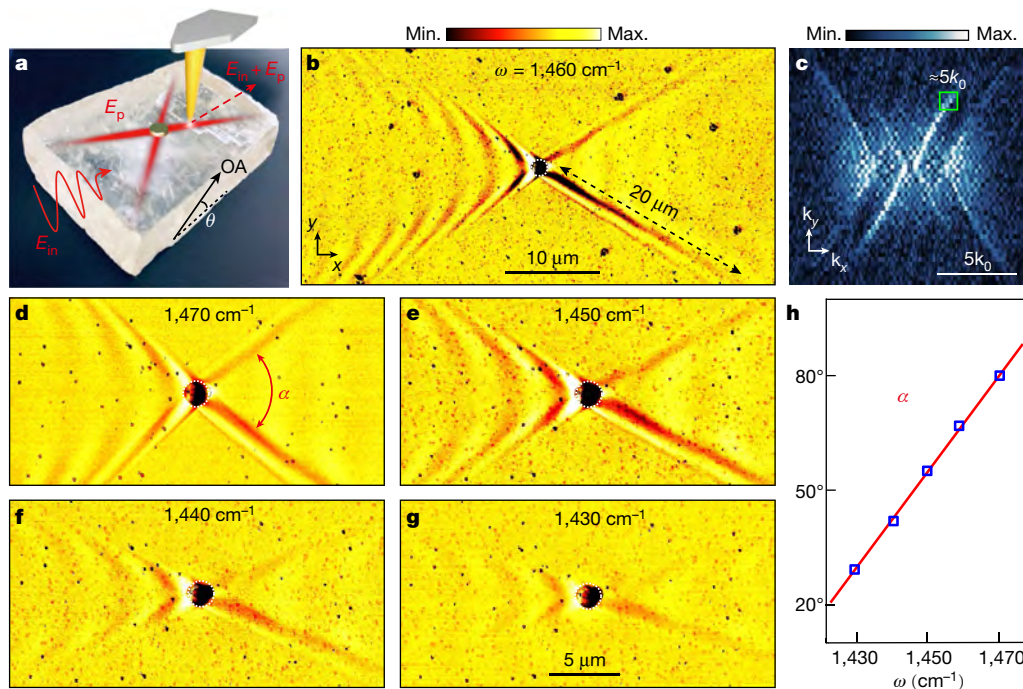


Fig. 2 | Real-space imaging of g-HPs excited by an infrared antenna under oblique plane-wave illumination at the surface of bulk calcite. **a**, Schematic of near-field imaging experiments (sample information in Extended Data Fig. 1). The disk nanoantenna concentrates p-polarized mid-infrared illumination (with an angle $\varphi = 30^\circ$ to the surface) into a local hotspot able to launch highly confined polaritons. The polariton field E_p propagates along the surface, interfering with the incident field E_{in} . The metallic tip of a scattering-type scanning near-field microscope (s-SNOM) records the interference field $E_{in} + E_p$ when the sample is scanned, yielding the near-field optical image of polariton fields with nanoscale resolution. **b**, Experimental

near-field image of antenna-launched g-HPs at the illuminating frequency $\omega = 1,460 \text{ cm}^{-1}$. The dashed line indicates the long distance travelled by the polariton rays (greater than $20 \mu\text{m}$). The diameter of the disk antenna is $D = 1.6 \mu\text{m}$. **c**, Absolute value of the Fourier transform of the image shown in **b**; scale bar is normalized to the photo wavevector k_0 . The green box indicates a component with wavevector $|k| \approx 5k_0$. **d–g**, Near-field images recorded at four more illuminating frequencies as indicated. The red arrow in **d** indicates the open angle α of g-HP rays. **h**, Frequency dependence of the open angle. Blue symbols are experimental data extracted from the images shown in **b**, **d–g**. The red line shows the simulation results (Supplementary Information section 2).

highlight the exotic nature of g-HPs, excluding the effect of a complex dielectric permittivity. The presence of realistic loss does not affect our main conclusions (Extended Data Fig. 4). The oblique wavefronts strongly depend on the orientation of the optic axis and the direction of in-plane wavevectors (Supplementary Fig. 1), yielding a marked reconfigurability of the polariton dispersion, as demonstrated below. These distinctive features reveal g-HPs as a unique surface electromagnetic mode that emerges in anisotropic crystals in which the optic axis is not aligned with the surface.

To directly probe g-HPs, we performed near-field imaging experiments to visualize real-space anisotropic polariton propagation along the surface (Fig. 2a). We fabricated a gold disk (diameter $D = 1.6 \mu\text{m}$) on the (100) surface of a bulk calcite substrate ($\theta = 23.3^\circ$) (Methods). The disk acts as an optical nanoantenna that concentrates p-polarized mid-infrared illumination (with an angle $\varphi = 30^\circ$ to the surface) into a local hot spot that is able to launch highly confined polaritons. Figure 2b presents the near-field image of disk-launched polaritons measured at $\omega = 1,460 \text{ cm}^{-1}$. The polaritons exhibit concave wavefronts on the left of the disk, consistent with the numerical simulations in Fig. 1b. In marked contrast, on the right we measure ray-like (diffraction-less) polaritonic patterns extending for a distance of at least $20 \mu\text{m}$ (3 times the photon wavelength). Such long distance is notable, and it represents—to our knowledge—a record length for in-plane hyperbolic polaritons, compared with previously observed values of around half of the photon wavelength in natural materials^{7,8}. Theoretical calculations also demonstrated that g-HPs exhibit lower loss compared with v-HPs and s-HPs (Supplementary Fig. 2). The formation of polariton rays can be explained by stronger local fields (thus larger local photonic density of states) generated on the right portion of the disk owing to the oblique

illumination (further discussion in Supplementary Fig. 3 and experimental results in Supplementary Fig. 4). Notably, we highlight that the propagation of g-HP rays is in marked contrast to that of a conventional polariton mode (single-mode wave). The g-HP rays are formed by the superposition of many polariton modes with different wavevectors, and effectively exhibit a strongly anisotropic wavevector dispersion. As a result, the g-HP rays can maintain high resolution, transferring the large- k information over a long distance without diffraction. We illustrate this mechanism in Extended Data Fig. 5. Our numerical simulations (with a plane wave source, incident angle $\varphi = 30^\circ$ consistent with the experiments) reproduce our experiments with excellent agreement (Extended Data Fig. 6); this confirms that the experimentally measured signals can be attributed to the disk and not to a tip launching effect (note that the simulations do not include the tip), as the polaritons launched by the tip are weakly reflected by the metal structure⁶.

The Fourier transform of the near-field image in Fig. 2b shows two different hyperbolic IFCs in k -space (Fig. 2c), corresponding to the left and right parts of Fig. 2b, respectively, mapped into the outer and inner IFCs (Supplementary Fig. 5). The difference between wavevectors (denoted as Δ) between the two IFCs stems from the asymmetric interference of the illuminating field and the polariton fields propagating on the antenna left and right sides (for example, for the k_x axis, the polariton propagating on the left side yields $k_{x,\text{left}} = k_x + \Delta/2$, the one propagating on the right side yields $k_{x,\text{right}} = k_x - \Delta/2$, $\Delta = 2k_0 \cos\varphi$ (refs. 34,35)). The polariton in-plane wavevectors are also experimentally quantified, $|k| > 5k_0$, and are larger than those of isotropic surface polaritons propagating over a single interface³⁴.

By altering the illumination frequency, we studied the frequency dependence of the anomalous ray-like propagation (Fig. 2d–g). Notably,

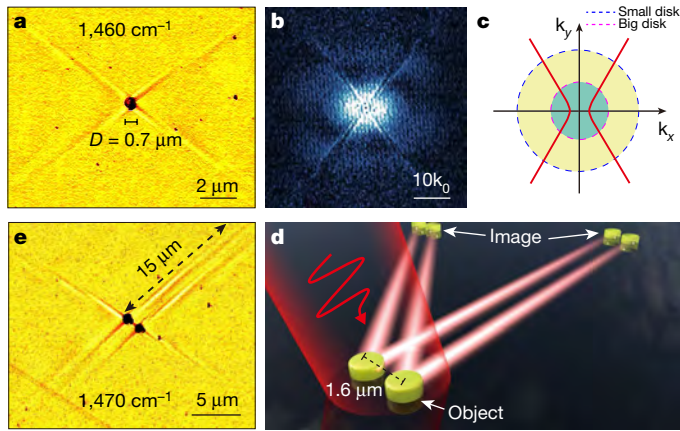


Fig. 3 | Launching highly confined g-HPs for in-plane directional and diffraction-less polariton propagation. **a**, Near-field image of large-wavevector g-HPs launched by a small antenna (diameter $D = 0.7 \mu\text{m}$), recorded at $\omega = 1,460 \text{ cm}^{-1}$. **b**, Absolute value of the Fourier transform of the image shown in **a**. **c**, Sketch of the strategy for reducing the antenna size for exciting large-wavevector g-HPs. **d**, Schematic of the g-HP-based directional and diffraction-less polaritons. **e**, Experimental verification of in-plane directional and diffraction-less polariton propagation. The centre-to-centre distance between the two disks is $1.6 \mu\text{m}$, and $D = 0.65 \mu\text{m}$. The two disks, the illumination and the optic axis are not aligned, which thus causes the asymmetric field distribution.

the open angle α of the polariton ray (definition in Fig. 2d) increases with the frequency, matching our numerical results (Fig. 2h). Indeed, all our experimental near-field images show an excellent agreement with numerical simulations (Extended Data Fig. 6), supporting the claim that we observe the g-HPs that we predict in Fig. 1.

The g-HPs feature long-distance ray-like propagation, as demonstrated in Fig. 2. Larger-wavevector (that is, more confined) g-HPs can be launched by a smaller sized disk. This scenario is studied in Fig. 3a,

in which we observe sharp polariton rays being launched on both sides of a small disk ($D = 0.7 \mu\text{m}$), in contrast to Fig. 2b. The more symmetric field distribution is explained by larger-wavevector polariton fields (illustrated in Fig. 3c), which are much less influenced by the illuminating field, given by the wavevector mismatch (namely, $|\mathbf{k}| \gg \Delta$, thus $k_{x,\text{left}} \approx k_{x,\text{right}} \approx |\mathbf{k}|$). The Fourier transform of Fig. 3a indeed corroborates the presence of polaritons with larger wavevector components—up to $21k_0$ (as shown in Supplementary Fig. 6)—because they are launched by a smaller antenna. Notably, despite the increased wavevectors, the g-HP rays still travel for a considerably longer distance (more than $15 \mu\text{m}$) than the v-HP rays that are observed in twisted van der Waals materials (approximately $3 \mu\text{m}$)²⁰.

The experimentally observed long-distance, highly confined, ray-like propagation of g-HPs suggests promise for applications in deeply subwavelength-scale information transfer³⁶. As an example, we demonstrate in-plane directional and diffraction-less polariton propagation to image subwavelength-scale objects. To this end, two gold disks were fabricated, which serve as the objects to be imaged ($1.6 \mu\text{m}$ centre-to-centre separation) on the (100) surface of a calcite substrate (schematic in Fig. 3d). The recorded near-field image (Fig. 3e) corroborates the fact that the two disks, excited by the external illumination, launch highly directional polaritonic rays that propagate along the sample surface. Notably, these rays indeed transfer the sub-wavelength information of the objects (for example, the width of the ray strictly equals the disk diameter) to a distance larger than $15 \mu\text{m}$.

Having established the exotic features of g-HPs and their applications via in-plane directional and diffraction-less polariton propagation, we discuss the dispersion engineering of calcite polaritons. Recently, it has been shown that the in-plane misalignment of optic axis facilitates fine control of polariton dispersion in twisted thin van der Waals materials^{20,37}. Here we demonstrate—by controlling the easily tunable crystallographic orientation (angle θ) of calcite—that the out-of-plane rotation of the optic axis can also manipulate the polariton propagation without requiring any heterostructure, demonstrating polariton-dispersion engineering in three dimensions. As illustrated in Fig. 4a, the angle θ

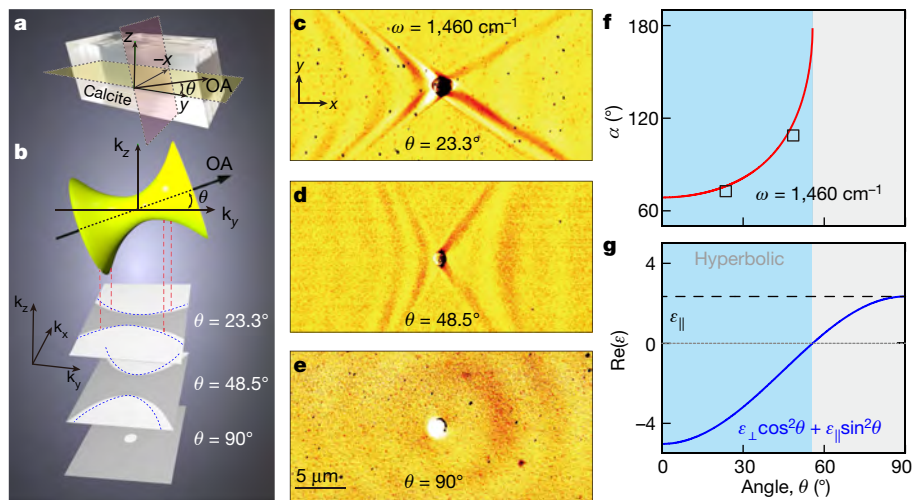


Fig. 4 | Tunable hyperbolicity and topological transition of polaritons in calcite. **a**, Schematic of a selective plane in calcite. Its optic axis is within y - z plane, the interface between the calcite and background is within the x - y plane, and the angle θ is defined between the y axis and the optic axis. The pale yellow surface corresponds to the characteristic plane (100) when $\theta = 23.3^\circ$, while the pale red surface is the characteristic plane (001) when $\theta = 90^\circ$. **b**, Schematic of projected in-plane isofrequency contour, at $\theta = 23.3^\circ$, 48.5° and 90° . The three-dimensional isofrequency surface (yellow surface) is projected to the k_x - k_y plane, with the grey regime denoting its shadow. When a mode with (k_x, k_y) locates within this shadow, the k_z should be real-valued, and the mode therein is

v-HPs. The g-HPs should only exist when a mode locates outside of its shadow and $0^\circ < \theta < 90^\circ$, the schematic IFC of g-HPs are represented by the blue dashed line. **c–e**, Experimental near-field amplitude images at $\omega = 1,460 \text{ cm}^{-1}$ with different tilted angles at $\theta = 23.3^\circ$ (**c**), $\theta = 48.5^\circ$ (**d**) and $\theta = 90^\circ$ (**e**). **f**, The experimentally measured open angle (α) of g-HPs (black square) plotted against the open angle of the shadow boundary of the projected three-dimensional isofrequency surface (red line). The g-HPs have a slightly smaller open angle. **g**, The plots of the two projected effective in-plane permittivities ($\epsilon_{||}$ and $\epsilon_{\perp} \cos^2 \theta + \epsilon_{||} \sin^2 \theta$) as a function of tilted angle θ at the frequency $\omega = 1460 \text{ cm}^{-1}$. The hyperbolic regime is marked by light blue.

can be effectively rotated by mechanically cutting the calcite crystal along different planes. For example, $\theta = 23.3^\circ$ is achieved via cutting along the plane (100), whereas $\theta = 90^\circ$ cuts along the plane (001). Varying the angle θ effectively rotates the bulk IFC of v-HPs in \mathbf{k} -space (Fig. 4b, top), accordingly altering its projection on the k_x – k_y plane (bottom, grey areas in Fig. 4b), which may affect the condition $\varepsilon_\perp \cos^2\theta + \varepsilon_\parallel \sin^2\theta < 0$ that is necessary to support g-HPs. The dispersion of g-HPs should be located outside that of bulk IFCs, or equivalently, the whole k_x – k_y plane cannot be filled by the projected bulk IFC. Otherwise, for any possible in-plane momentum (k_x , k_y), the out-of-plane momentum is always real-valued, and the g-HPs with complex out-of-plane momentum cannot be supported (Supplementary Information section 1). As a result, the g-HPs—with their in-plane IFCs marked as the blue dashed line in Fig. 4b, close to but different from the bulk IFC projection—can also be controlled by the angle θ .

As an experimental demonstration of crystallography-induced tunability of the g-HP dispersion, we show near-field images at $\omega = 1,460 \text{ cm}^{-1}$ on three calcite samples with different optic axis orientations ($\theta = 23.3^\circ$, 48.5° and 90° , Fig. 4c–e, respectively). The detailed sample information is shown in Extended Data Fig. 1. When $\theta = 23.3^\circ$ and $\theta = 48.5^\circ$, the polariton exhibits anisotropic (hyperbolic) in-plane propagation (Fig. 4c, d, Supplementary Figs. 5, 7). The open angle α of the polariton rays increases with θ (Fig. 4f), in agreement with our theoretical model. On the other hand, we observe circular (isotropic) polariton propagation on the sample with $\theta = 90^\circ$ (Fig. 4e, Supplementary Fig. 8). This corresponds to a topological transition, in which polaritons transition from open hyperbolic to closed circular dispersions. As shown in Fig. 4g, varying θ results in a sign change of $\varepsilon_\perp \cos^2\theta + \varepsilon_\parallel \sin^2\theta$ from negative to positive, thus breaking the necessary condition for the existence of g-HPs. Specifically, at $\omega = 1,460 \text{ cm}^{-1}$, the g-HPs can only exist in the range below the critical angle (approximately 57°). For larger angles, in-plane isotropic polariton modes are found on the surface (Fig. 4e, Supplementary Fig. 8). This tunability is robust and can also be found at other frequencies, as shown in Supplementary Fig. 9. Therefore, in combination with the recent observation of polariton topological transitions via in-plane optic axis alignment^{20,37}, our demonstration of optic axis out-of-plane orientation in bulk calcite crystals shows how simple geometrical arguments can guide extreme dispersion engineering of polaritons supported in polar anisotropic materials.

Although we demonstrated g-HPs in calcite, these polaritons can also emerge in other natural anisotropic crystals—for example quartz³⁸ and sapphire³⁹. Our results also show that conventional bulk anisotropic crystals are excellent candidates for exploring exotic polariton anisotropy, in addition to two-dimensional layered van der Waals materials and hyperbolic metamaterials that have recently drawn considerable attention. Owing to three-dimensional nature, bulk anisotropic crystals provide an additional means in which to support and control exotic polariton waves for applications in imaging, bio-sensing, light guiding, information transfer, infrared polarization elements and enhanced nonlinearity at a deeply subwavelength scale.

Online content

Any methods, additional references, Nature Research reporting summaries, source data, extended data, supplementary information, acknowledgements, peer review information; details of author contributions and competing interests; and statements of data and code availability are available at <https://doi.org/10.1038/s41586-021-03755-1>.

- Basov, D. N., Fogler, M. M. & Garcia de Abajo, F. J. Polaritons in van der Waals materials. *Science* **354**, aag1992 (2016).
- Low, T. et al. Polaritons in layered two-dimensional materials. *Nat. Mater.* **16**, 182–194 (2017).

- Hu, G., Shen, J., Qiu, C.-W., Alù, A. & Dai, S. Phonon polaritons and hyperbolic response in van der Waals materials. *Adv. Opt. Mater.* **8**, 1901393 (2020).
- Dai, S. et al. Tunable phonon polaritons in atomically thin van der Waals crystals of boron nitride. *Science* **343**, 1125–1129 (2014).
- Caldwell, J. D. et al. Sub-diffractive volume-confined polaritons in the natural hyperbolic material hexagonal boron nitride. *Nat. Commun.* **5**, 5221 (2014).
- Li, P. et al. Infrared hyperbolic metasurface based on nanostructured van der Waals materials. *Science* **359**, 892–896 (2018).
- Ma, W. et al. In-plane anisotropic and ultra-low-loss polaritons in a natural van der Waals crystal. *Nature* **562**, 557–562 (2018).
- Zheng, Z. et al. A mid-infrared biaxial hyperbolic van der Waals crystal. *Sci. Adv.* **5**, eaav8690 (2019).
- Taboada-Gutiérrez, J. et al. Broad spectral tuning of ultra-low-loss polaritons in a van der Waals crystal by intercalation. *Nat. Mater.* **19**, 964–968 (2020).
- Sternbach, A. J. et al. Programmable hyperbolic polaritons in van der Waals semiconductors. *Science* **371**, 617–620 (2021).
- Alfaro-Mozaz, F. J. et al. Nanoimaging of resonating hyperbolic polaritons in linear boron nitride antennas. *Nat. Commun.* **8**, 15624 (2017).
- Giles, A. J. et al. Ultralow-loss polaritons in isotopically pure boron nitride. *Nat. Mater.* **17**, 134–139 (2018).
- Li, P. et al. Collective near-field coupling and nonlocal phenomena in infrared-phononic metasurfaces for nano-light canalization. *Nat. Commun.* **11**, 3663 (2020).
- Li, P. et al. Hyperbolic phonon-polaritons in boron nitride for near-field optical imaging and focusing. *Nat. Commun.* **6**, 7507 (2015).
- Dai, S. et al. Subdiffractive focusing and guiding of polaritonic rays in a natural hyperbolic material. *Nat. Commun.* **6**, 6963 (2015).
- Tielrooij, K.-J. et al. Out-of-plane heat transfer in van der Waals stacks through electron-hyperbolic phonon coupling. *Nat. Nanotechnol.* **13**, 41–46 (2018).
- Autore, M. et al. Boron nitride nanoresonators for phonon-enhanced molecular vibrational spectroscopy at the strong coupling limit. *Light Sci. Appl.* **7**, 17172 (2018).
- Bylinkin, A. et al. Real-space observation of vibrational strong coupling between propagating phonon polaritons and organic molecules. *Nat. Photon.* **15**, 197–202 (2021).
- Castilla, S. et al. Plasmonic antenna coupling to hyperbolic phonon-polaritons for sensitive and fast mid-infrared photodetection with graphene. *Nat. Commun.* **11**, 4872 (2020).
- Hu, G. et al. Topological polaritons and photonic magic angles in twisted α -MoO₃ bilayers. *Nature* **582**, 209–213 (2020).
- Li, P. et al. Optical nanoimaging of hyperbolic surface polaritons at the edges of van der Waals materials. *Nano Lett.* **17**, 228–235 (2017).
- Dai, S. et al. Manipulation and steering of hyperbolic surface polaritons in hexagonal boron nitride. *Adv. Mater.* **30**, 1706358 (2018).
- D'yakonov, M. New type of electromagnetic wave propagating at an interface. *Sov. Phys. JETP* **67**, 714–716 (1988).
- Narimanov, E. Ghost resonance in anisotropic materials: negative refractive index and evanescent field enhancement in lossless media. *Adv. Photonics* **1**, 056003 (2019).
- Waseer, W. I., Naqvi, Q. A. & Mughal, M. J. Non-uniform plane waves (ghost waves) in general anisotropic medium. *Opt. Commun.* **453**, 124334 (2019).
- Narimanov, E. Dyakonov waves in biaxial anisotropic crystals. *Phys. Rev. A (Coll. Park)* **98**, 013818 (2018).
- Narimanov, E. Electromagnetic Ghost Waves. in *Conference on Lasers and Electro-Optics JTu2A.144* (Optical Society of America, 2018).
- Walker, D., Glytsis, E. & Gaylord, T. Surface mode at isotropic–uniaxial and isotropic–biaxial interfaces. *J. Opt. Soc. Am. A* **15**, 248–260 (1998).
- Kuš, M., Haake, F. & Delande, D. Prebifurcation periodic ghost orbits in semiclassical quantization. *Phys. Rev. Lett.* **71**, 2167–2171 (1993).
- Zhou, S., Zhang, Q., Fu, S. F. & Wang, X. Z. Ghost surface phononic polaritons in ionic-crystal metamaterial. *J. Opt. Soc. Am. B* **35**, 2764–2769 (2018).
- Frech, R. & Nichols, H. Infrared reflectivity of calcite: Oblique phonons. *Phys. Rev. B* **17**, 2775–2779 (1978).
- Hellwege, K. H., Lesch, W., Plihal, M. & Schaack, G. Zwei-phononen-absorptionsspektren und dispersion der schwingungszweige in kristallen der kalkspatstruktur. *Z. Physik* **232**, 61–86 (1970).
- Breslin, V. M., Ratchford, D. C., Giles, A. J., Dunkelberger, A. D. & Owrutsky, J. C. Hyperbolic phonon polariton resonances in calcite nanopillars. *Opt. Express* **29**, 11760–11772 (2021).
- Huber, A., Ocelic, N., Kazantsev, D. & Hillenbrand, R. Near-field imaging of mid-infrared surface phonon polariton propagation. *Appl. Phys. Lett.* **87**, 081103 (2005).
- Huber, A. J., Ocelic, N. & Hillenbrand, R. Local excitation and interference of surface phonon polaritons studied by near-field infrared microscopy. *J. Microsc.* **229**, 389–395 (2008).
- Zhang, Q. et al. Interface nano-optics with van der Waals polaritons. *Nature* (in the press).
- Hu, G., Krasnok, A., Mazon, Y., Qiu, C.-W. & Alù, A. Moiré hyperbolic metasurfaces. *Nano Lett.* **20**, 3217–3224 (2020).
- Schuller, E., Borstel, G. & Falge, H. J. Surface phonon-polaritons on general crystal cuts of α -quartz observed by attenuated total reflection. *Phys. Status Solidi B* **69**, 467–476 (1975).
- Lee, S. C., Ng, S. S., Hassan, H. A., Hassan, Z. & Dumelow, T. Surface phonon polariton responses of hexagonal sapphire crystals with non-polar and semi-polar crystallographic planes. *Opt. Lett.* **39**, 5467–5470 (2014).

Publisher's note Springer Nature remains neutral with regard to jurisdictional claims in published maps and institutional affiliations.

© The Author(s), under exclusive licence to Springer Nature Limited 2021

Methods

Numerical simulations

Permittivity of the calcite crystal used in simulations. The uniaxial permittivity ($\epsilon_{\text{calcite},\perp}$ for the component in the direction perpendicular to the optic axis, $\epsilon_{\text{calcite},\parallel}$ for parallel to the optic axis) of the calcite crystal was calculated by Lorentz oscillator models, where two Lorentz oscillators were used for ϵ_{\perp} and one oscillator for ϵ_{\parallel} according to

$$\epsilon_{\perp} = \epsilon_{\infty,1} \left(1 + \frac{\omega_{\text{TO},1}^2 - \omega_{\text{TO},1}^2}{\omega_{\text{TO},1}^2 - \omega^2 - i\omega\Gamma_1} + \frac{\omega_{\text{LO},2}^2 - \omega_{\text{TO},2}^2}{\omega_{\text{TO},2}^2 - \omega^2 - i\omega\Gamma_2} \right) \quad (3)$$

$$\epsilon_{\parallel} = \epsilon_{\infty,3} \left(1 + \frac{\omega_{\text{LO},3}^2 - \omega_{\text{TO},3}^2}{\omega_{\text{TO},3}^2 - \omega^2 - i\omega\Gamma_3} \right) \quad (4)$$

ω_{TO} and ω_{LO} are the TO (transverse) and LO (longitudinal) phonon frequencies, respectively. Γ is the damping constant. ϵ_{∞} is the high-frequency permittivity. For ϵ_{\perp} , we took $\epsilon_{\infty,1} = 2.7$, $\omega_{\text{TO},1} = 712 \text{ cm}^{-1}$; $\omega_{\text{LO},1} = 715 \text{ cm}^{-1}$; $\Gamma_1 = 5 \text{ cm}^{-1}$. $\omega_{\text{TO},2} = 1,410 \text{ cm}^{-1}$; $\omega_{\text{LO},2} = 1,550 \text{ cm}^{-1}$; $\Gamma_2 = 10 \text{ cm}^{-1}$. For ϵ_{\parallel} , we took $\epsilon_{\infty,3} = 2.4$, $\omega_{\text{TO},3} = 871 \text{ cm}^{-1}$; $\omega_{\text{LO},3} = 890 \text{ cm}^{-1}$; $\Gamma_3 = 3 \text{ cm}^{-1}$. The parameters above are from ref.³². For best matching of our simulated and experimental results (Extended Data Fig. 6), we slightly changed the value from that given in ref.³² and used $\Gamma_1 = 5 \text{ cm}^{-1}$; $\omega_{\text{TO},2} = 1,410 \text{ cm}^{-1}$, $\omega_{\text{LO},2} = 1,550 \text{ cm}^{-1}$; $\omega_{\text{TO},3} = 871 \text{ cm}^{-1}$, $\Gamma_3 = 3 \text{ cm}^{-1}$ and we noted that the permittivities of calcite we used here are similar to the model in other work⁴⁰.

Information on general simulations. We used a finite-element numerical simulation software (COMSOL) to simulate near-field distributions of polaritons propagating along the surface of the calcite. The mode solver module of COMSOL was used for the quasi-normal mode analysis of g-HPs. Simulation details for each figure can be found in Supplementary Information section 2.

Materials and fabrication

We used large-sized calcite substrates (size: $1\text{cm} \times 1\text{cm}$; 1-mm-thick; different optic axis-orientation angles; Extended Data Fig. 1) commercially available, which were prepared by mechanical cleavage from bulk calcite single crystals (trigonal structures). Atomic force microscope (AFM) characterized the nanoscale smoothness of all the calcite substrates. Gold disk antennas were fabricated on the calcite surface via standard electron beam lithography. The disk patterns were written on the resist (PMMA: 495/A4, thickness $\approx 100 \text{ nm}$) spin-coated on the calcite substrate. The standard lift-off procedure was used after the e-beam evaporation of Ti (3 nm)/Au (40 nm) onto the developed resist.

s-SNOM measurements

For near-field imaging experiments, we used a s-SNOM system commercial from Neaspec based on an atomic force microscope

(AFM). The Pt-coated AFM tip oscillates vertically with an amplitude of about 50 nm at a frequency $\Omega \approx 270 \text{ kHz}$. It is illuminated by light from a wavelength-tunable continuous-wave quantum cascade laser ($1,310\text{--}1,470 \text{ cm}^{-1}$). The backscattered light is collected with a pseudo-heterodyne interferometer⁴¹. To suppress background contribution in the tip-scattered field, the interferometric detector signal is demodulated at a higher harmonic $n\Omega$ ($n \geq 2$), yielding near-field amplitude s_n and phase ϕ_n images. Figures 2–4 show amplitude s_2 images.

Data availability

The data that support the findings of this study are available from the corresponding authors upon reasonable request.

Code availability

The code that support the findings of this study are available from the corresponding authors upon reasonable request.

40. Lane, M. D. Midinfrared optical constants of calcite and their relationship to particle size effects in thermal emission spectra of granular calcite. *J. Geophys. Res. Planets* **104**, 14099–14108 (1999).
41. Ocelic, N., Huber, A. & Hillenbrand, R. Pseudoheterodyne detection for background-free near-field spectroscopy. *Appl. Phys. Lett.* **89**, 101124 (2006).

Acknowledgements We acknowledge support from T. Wang for micro-FTIR measurements, and Y. F. Hao and Y. S. Wang for antenna fabrication. P.L. acknowledges the support from the National Natural Science Foundation of China (grant no. 62075070). C.-W.Q. acknowledges support from the National Research Foundation, Prime Minister's Office, Singapore, under its Competitive Research Programme (CRP award NRF CRP22-2019-0006) and from grant R-261-518-004-720 from the Advanced Research and Technology Innovation Centre (ARTIC). G.H. acknowledges support from A*STAR under its AME Young Individual Research Grants (YIRG, no. A2084c0172). A.A. acknowledges support from the Office of Naval Research (grant no. N00014-19-1-2011), the Simons Foundation, the Air Force Office of Scientific Research MURI program, and the Department of Defense Vannevar Bush Faculty Fellowship. Q.D. acknowledges support from the National Natural Science Foundation of China (grant no. 51925203). D.H. acknowledges support from the National Natural Science Foundation of China (grant no. 11704085). X.Z. acknowledges support from the National Key Research and Development Program of China (grant no. 2018YFA0704403).

Author contributions C.-W.Q. and P.L. conceived the study. W.M. fabricated the samples. G.H. performed the theory analysis coordinated by C.-W.Q. and A.A. D.H. and W.M. performed the s-SNOM measurements with the help of T.S. and Y.Z. G.H., R.C. and W.M. performed the simulations. P.L., C.-W.Q., A.A., Q.D. and X.Z. coordinated and supervised the work. W.M., G.H., A.A., C.-W.Q. and P.L. wrote the manuscript with input from all co-authors.

Competing interests The authors declare no competing interests.

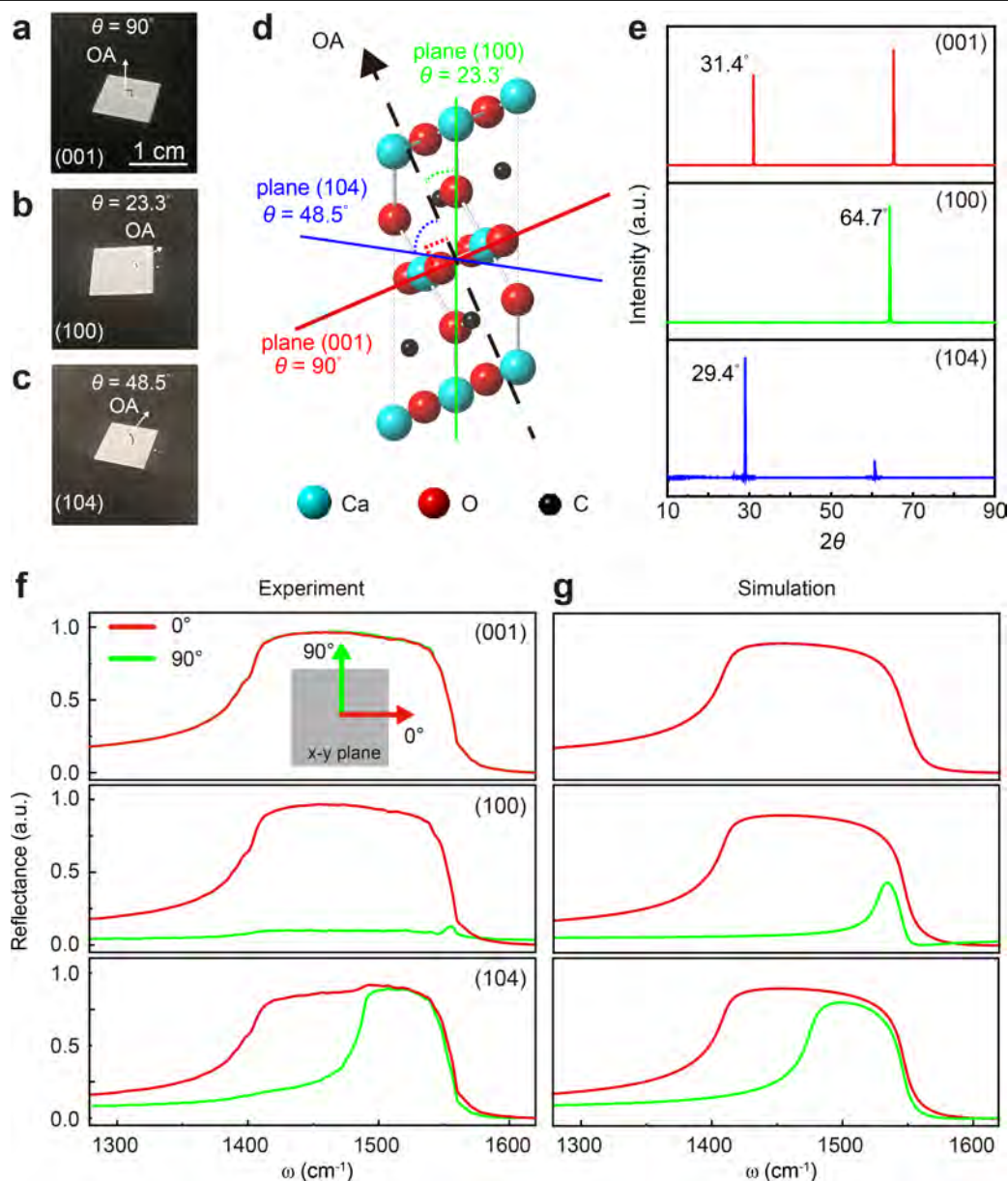
Additional information

Supplementary information The online version contains supplementary material available at <https://doi.org/10.1038/s41586-021-03755-1>.

Correspondence and requests for materials should be addressed to X.Z., Q.D., A.A., C.-W.Q. or P.L.

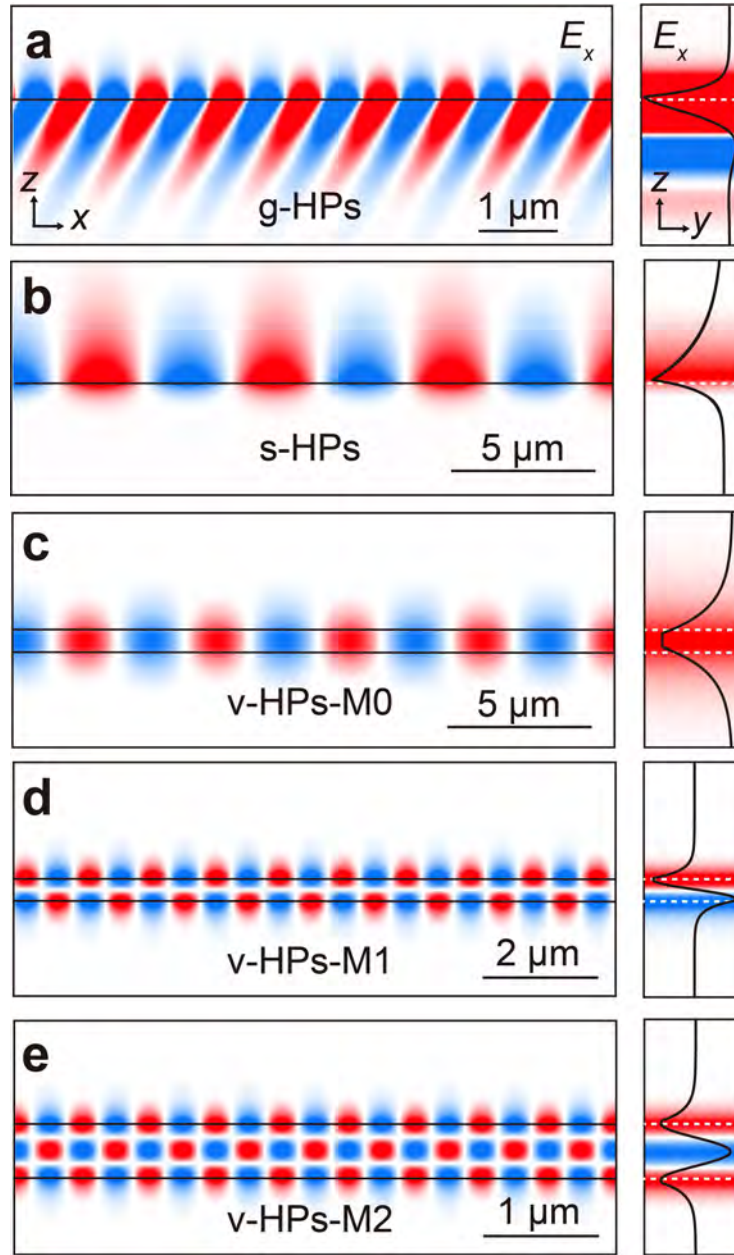
Peer review information *Nature* thanks Thomas Folland and the other, anonymous, reviewer(s) for their contribution to the peer review of this work.

Reprints and permissions information is available at <http://www.nature.com/reprints>.



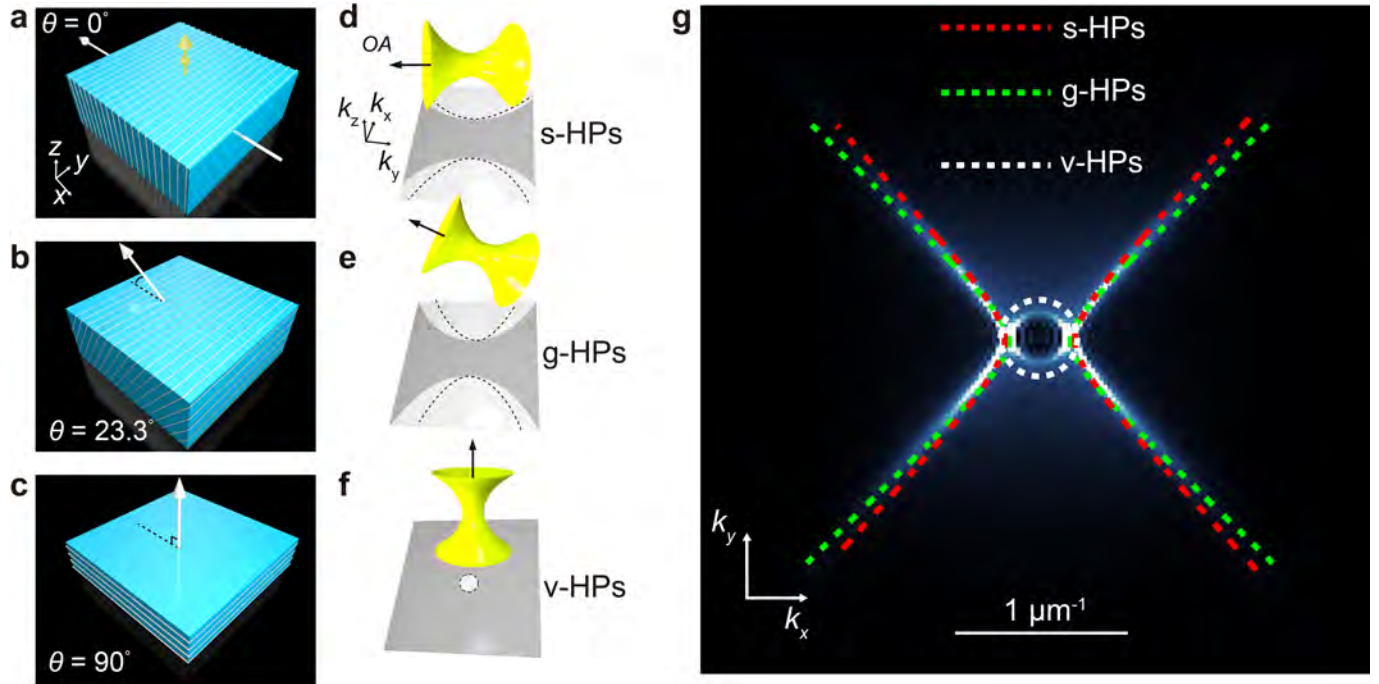
Extended Data Fig. 1 | Centimetre-sized calcite substrates with different optic axis-orientations and corresponding XRD patterns, angle-resolved far-field reflectance. **a–c**, Optical microscope images of calcite substrates for $\theta = 90^\circ$, 23.3° , 48.5° (the crystal surface is along plane (001), (100), (104), respectively). **d**, Schematics of the characteristic planes and the corresponding angle θ with respect to optic axis. Black dashed arrow represents optic axis. Green, red and blue lines indicate the characteristic plane (100), (001), (104), respectively. **e**, X-ray diffraction (XRD) data of calcite substrates with different angles with respect to optic axis. XRD patterns of three calcite substrates with

different θ exhibited strong diffraction peaks at 31.4° , 64.7° , 29.4° indicating the characteristic plane (001), (100) and (104) of calcite, respectively. **f**, Fourier-transform infrared reflection spectra of calcite substrates shown in **a–c** for different polarization angles of the incident light. The 0° polarization defined here is parallel with direction of red arrow in *x-y* plane. **g**, Theoretically fitted spectra using the dielectric permittivities according to Methods. The results for the calcite substrates for $\theta = 90^\circ$ (the surface is along plane (001)), $\theta = 23.3^\circ$ (the surface is along plane (100)) and $\theta = 48.5^\circ$ (the surface is along plane (104)), respectively.



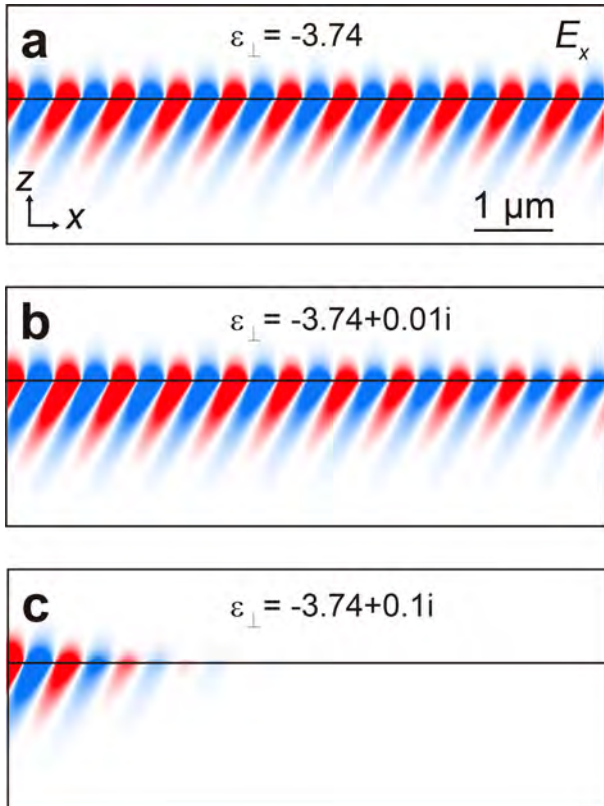
Extended Data Fig. 2 | Comparison of the modal patterns of the g-HPs, s-HPs and v-HPs. a–c, Transverse cross-section of the simulated near-field distributions of a g-HPs mode (a), s-HPs mode (b) and the fundamental v-HPs waveguide mode M0 (c). These results are shown in Fig. 1. **d, e,** Near-field distributions of the higher order v-HPs waveguide modes, M1 (d) and M2 (e). The s-HPs possess pure imaginary-valued k_z and thus exponentially decay inside the crystal. The v-HPs exhibiting real-valued wave vector k_z in the

material. They thus can accumulate the phase variations in the vertical direction to form Fabry–Pérot interferences between the two interfaces, resulting in the different order waveguide modes. By contrast, as a consequence of the oblique wavefronts, the g-HPs exhibit an unusual propagation feature: their electric fields exponentially attenuate with sinusoidal phase oscillations inside calcite.

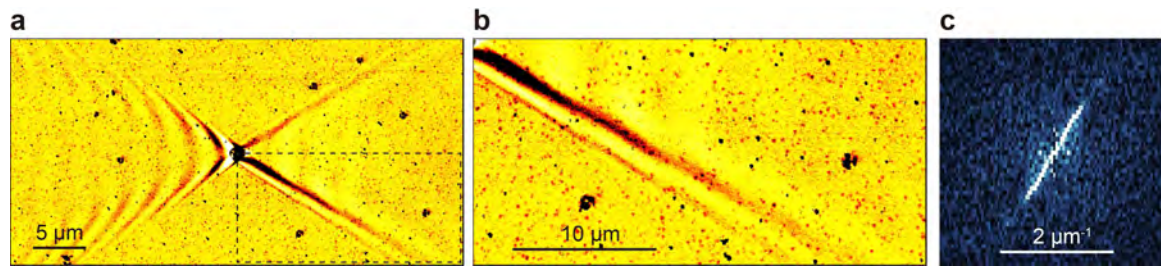


Extended Data Fig. 3 | Comparison of in-plane polariton dispersion for s-HPs, g-HPs and v-HPs. **a–c**, Schematic illustration of bulk calcite crystal with $\theta = 0^\circ, 23.3^\circ, 90^\circ$. **d–f**, Natural crystals can exhibit extreme dielectric anisotropy, arising when the permittivity tensor elements along orthogonal principal axes have opposite signs (for example, either type I: $\text{Re}(\epsilon_\perp) > 0, \text{Re}(\epsilon_\parallel) < 0$, or type II: $\text{Re}(\epsilon_\perp) < 0, \text{Re}(\epsilon_\parallel) > 0$, for uniaxial materials^{4,5}). These features result in polaritons—light–matter hybrid electromagnetic excitations—with a hyperbolic dispersion, that is, the polariton wavevector \mathbf{k} can support the hyperbolic isofrequency contours. Because of the two types of anisotropic dielectric permittivity, the hyperbolic dispersions are accordingly in the form of two types of open hyperboloids, which are the solutions of the equation of the

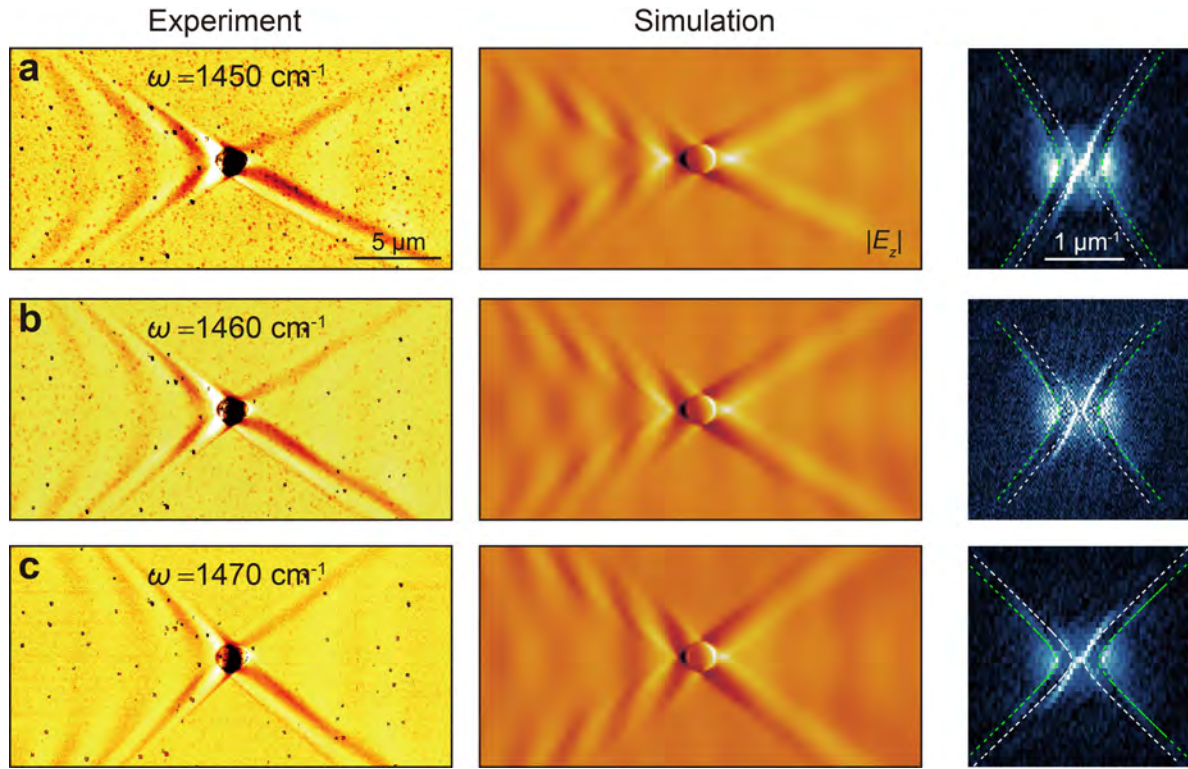
wavevector \mathbf{k} given by $k_x^2/\epsilon_\perp + (k_y^2 + k_z^2)/\epsilon_\parallel = k_0^2$, in which k_0 is the free-space wavevector. As a result, the polaritons in strongly anisotropic materials are called hyperbolic polaritons^{1–3}. The figure shows schematic illustrations of three-dimensional isofrequency and projected in-plane isofrequency contours (represented by the blue dashed line) at the k_x – k_y plane for s-HPs (**d**), g-HPs (**e**) and v-HPs (**f**) at the corresponding angle $\theta = 0^\circ, 23.3^\circ, 90^\circ$. The black dashed arrow represents the optic axis. **g**, A false-colour map showing the Fourier transform results of dipole-launched g-HPs. Dashed red, green and white lines correspond to the theoretical IFCs of in-plane wave vectors for s-HPs, g-HPs and v-HPs respectively.



Extended Data Fig. 4 | Numerical simulations of g-HPs considering the material loss. a–c, Transverse cross-section of the simulated near-field distribution of a g-HP mode for different losses. It is clear that the g-HPs still exist in the presence of the loss. However, the propagation length is reduced when adding the loss. For all cases we use $\epsilon_{\parallel} = 2.34$.



Extended Data Fig. 5 | Evaluation of the effective wavevectors of g-HP rays. **a**, Near-field image of antenna-launched g-HPs, shown in Fig. 2b. **b**, Magnified image of the g-HP ray, taken from the area marked in **a**. **c**, Fourier transform of **b**, indicating the composite of the super-composed mode.



Extended Data Fig. 6 | Comparison of experimental and simulated near-field images of disk-launched g-HPs. a–c. Disk-launched g-HPs at three different frequencies: $\omega = 1,450 \text{ cm}^{-1}$ (**a**), $\omega = 1,460 \text{ cm}^{-1}$ (**b**) and $\omega = 1,470 \text{ cm}^{-1}$ (**c**). Left, experimental near-field images of g-HPs. Middle, simulated near-field images of disk-launched g-HPs. Right, Fourier transform of the experimental

near-field images shown in the left panels. Green and white lines are theoretical IFCs of in-plane wave vectors by considering the interference factors ($\pm k_0 \cos \varphi$) according to Supplementary Fig. 3. Considering that the metallic s-SNOM tip is not included in the calculations, we thus assign the experimental near-field distribution to disk-launched polaritons.